He Huang[1,2], Xuzhang Shen[1,2*], Jian Xu[1,2], Rui Gao[1,2], Wentian Wang[1,2], Qiming Zhou[1,2], and Qiangqiang Huang[1,2]

[1] Guangdong Provincial Key Laboratory of Geodynamics and Geohazards, School of Earth Sciences and Engineering, Sun Yat-Sen University, Guangzhou 510275, China.

[2] Southern Marine Science and Engineering Guangdong Laboratory (Zhuhai), Zhuhai 519082, China.

Corresponding author: Xuzhang Shen (shenxzh5@sysu.edu.cn)

Key Points:

- A short-period dense seismic array in the southwest Cathaysia block
- The slight uplift of Moho towards the coastal area
- Abnormal deepen Moho and high Vp/Vs ratio beneath the Sanshui basin

Abstract

To better constrain the amalgamation of the East and West Cathaysia blocks, we deployed a short-period dense seismic array oriented nearly north-south in the southwestern Cathaysia block. According to the 997 teleseismic receiver functions recorded by 527 node geophones, we find that the Mohorovicic discontinuity (Moho) is slightly uplifted towards the coastal Cathaysia block. The most obvious feature is the high Vp/Vs ratio and deepen Moho beneath the Sanshui basin. Based on the common conversion point (CCP) migration images, we deduce that there may be distributed with the extension of the Gaoyao-Huilai deep fault, and it is supported by the offset of Moho and occurrence of the Mw 4.3 earthquake. Combined with other evidences, we further concluded that a weak suture zone is constrained beneath along the Zhenghe–Dapu and Gaoyao–Huilai deep faults, which may indicate the remnants of the amalgamation of the East and West Cathaysia blocks.

Plain Language Summary

In recent years, with the development of short-period dense array, people can detect many fine crustal structures, which is an important milestone in the development of seismology observations. Using a short-period dense seismic array deployed in the Cathaysia block, we obtained an unprecedented detailed profile from Zhuhai to Lianzhou City in Guangdong Province, China. Depending on this, we find that the abnormal deepen and offset Moho beneath the Sanshui basin may indicate the deep extension of the Gaoyao-Huilai deep fault. The occurrence of a 4.3Mw earthquake provides this interpretation with certain evidence. The new finding from our research provides good constrain for the remnants of amalgamation of the East and West cathaysian block in the southwest Chathaysia block, and which has not been reported before.

1 Introduction

1.1 Tectonic setting of the South China block

The South China block (SCB), located near the southeastern edge of the Eurasian plate, is believed to have been assembled following the Neoproterozoic collision between the Yangtze and Cathaysia blocks along the Jiangnan orogenic belt (Zhao & Cawood, 2012) (Fig 1 b). The Cathaysia block located in the southeastern SCB is broadly divided into the East and West Cathaysia blocks by the Gaoyao–Huilai and Zhenghe–Dapu faults. Three main tectonic events (the Jinningian event at ~970 Ma, the Caledonian event at ~420 Ma, and the Indosinian event at ~230 Ma) have been proposed based on outcrops of metamorphic rocks to account for the complex tectonic history of the SCB. Recently, researchers favored that the above events may have been driven mainly by the closure of the Paleo-South China Sea, Proto-Tethys and Paleo-Tethys Oceans, and Paleo-Pacific Ocean, respectively (Shu et al., 2021). In particular, the subduction of the Paleo-Pacific plate and cycle of slab advance and retreat, including the initiation of subduction, the occurrence of flat subduction, and slab rollback (Li & Li, 2007), played important roles in the widespread distribution of mid-late Mesozoic metamorphic and igneous rocks throughout the Cathaysia block (Jiang et al., 2015).

The well-known Jinningian event may represent the collision between the Yangtze and Cathaysia blocks, and characterized by a double subduction model along the Jiangshan Orogenic belt (Zhao, 2015) . In response to the amalgamation of the North China block with the SCB, the Caledonian tectonothermal event is indicated by granite gneissic rock ($^{206}Pb/^{238}U$ apparent age of 421–441 Ma) in the Wuyi–Yunkai domain within the southeastern Cathaysia block (Wang et al., 2007). The Mesozoic granites formed by partial melting of the upper and middle crust may caused from the extensive Indosinian and Yanshanian metamorphic rocks in the Cathaysia block (weighted mean $^{206}Pb/^{238}U$ age of ~236 Ma) Zhou (2003). Nevertheless, considering that S-type granites correlate with the melting of the middle or upper crust while I-type granites correlate with the melting of the lower crust (Tang et al., 2021), the petrogenesis of different types of granites in the Cathaysia block is still disputed. Specifically, some arguments focus on whether outcrops of metamorphic rocks are associated with an intraplate orogeny or subduction-collision processes. In this consuptions, Liu et al. (2018) support an oceanic subduction and accretion genesis hypothesis, whereas other groups support intraplate orogenesis (460–400 Ma) (Huang et al., 2013; Tang et al., 2021; Yu et al., 2018). However, without high-resolution data, there is no direct evidence supporting the amalgamation of the East and West Cathaysia blocks, especially in the southwestern portion of the Cathaysia block.

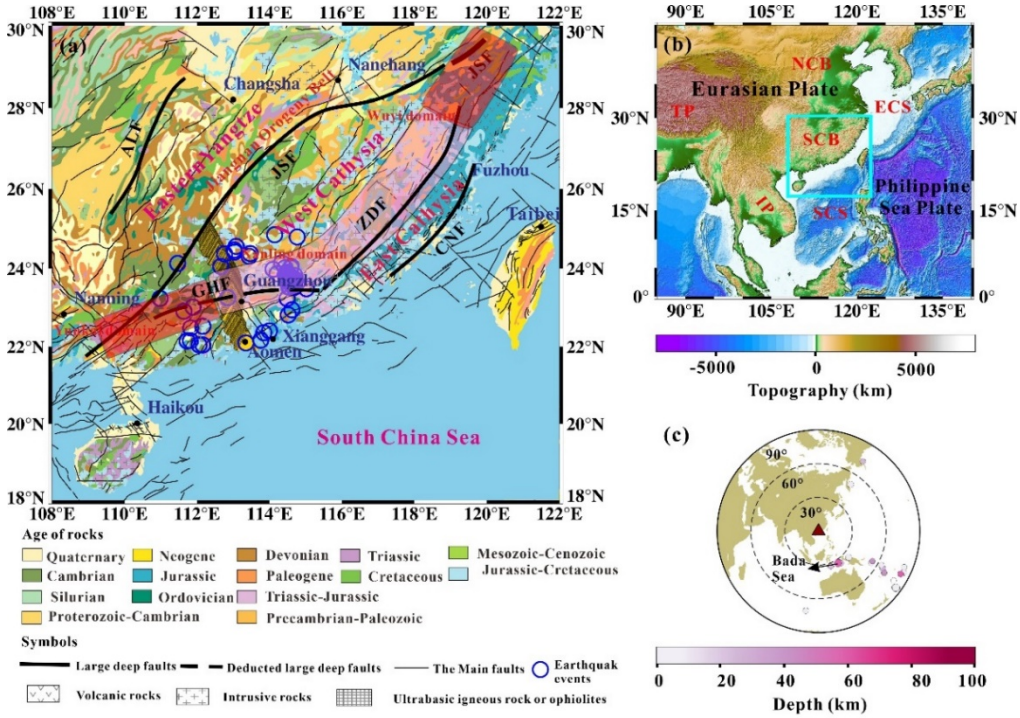

Figure 1. (a) Tectonic setting of the SCB. The different colours in the background indicate the different periods of rock outcrops distributed throughout the SCB. The thick solid lines represent the convergence boundary and deep faults between blocks: GHF: Gaoyao–Huilai fault; ZDF: Zhenghe–Dapu fault; ALF: Anhua–Luocheng fault; CNF: Changle–Nanao fault; JSF: Jiangshao-Shaoxing fault. The thick dashed lines are the inferred boundaries between blocks. The thin black lines are major faults in mainland China, while the blue circles denote Mw 3.0 earthquakes that occurred from 1980 to 2021 downloaded from the Incorporated Research Institutions for Seismology (IRIS) website (http://ds.iris.edu/ieb/). The gold triangles represent the node geophones deployed along the Zhuhai–Lianzhou profile. (b) Tectonic setting of Southeast Asia. The equilateral blue rectangle denotes the main research area in panel (a). NCB: North China block; SCB: South China block; ECS: East China Sea; SCS: South China Sea; TP: Tibetan Plateau; IB: Indochina block. (c) Teleseismic events recorded by the node geophones. The dark red triangle indicates the location of the dense array in Guangdong Province, China. The circles of different sizes are the teleseismic events recorded by the dense seismic array with epicentral distances within 30~90° and Mw 5.0. The Mw 7.3 Banda Sea earthquake (black arrow) occurred on 24 June 2019 at 02:53:39 (Coordinated Universal Time, UTC) at an epicentral distance of 212.0 km (33.57°).

1.2 The dense short-period seismic array

The detection of fine subsurface structures in modern seismology always requires a good sampling frequency in the spatial domain, which may be beyond the ability of most permanent seismic stations with a large spacing of 20~100 km (Shen et al., 2019). Meanwhile, these permanent stations can be supplemented by deploying portable broadband stations with a small spacing of 1~20 km (Wang et al., 2018; Ye et al., 2017; Yuan et al., 1997; Zhu, 2000). However, broadband stations are expensive and thus are sparsely adopted, while the resolution depending on the spacing between two stations is limited. In recent years, with the development of dense short-period seismic arrays with intervals ranging approximately from 100 m to 2 km, fine crustal structures have been discovered in increasingly observations.

In the early studies, Yuan et al. (1997) proposed the moveout correction methods based on the INDEPTH short-period seismic array, and Zhu (2000) developed the common conversion point (CCP) migration method based on the LARSE short-period seismic array. More recently, based on 473 seismometers, Shen et al. (2020) suggested that a pure shear shortening model beneath the Qilian Mountains can explain the lateral growth of the northern front of the Tibetan Plateau. Moreover, based on a dense array of 340 seismometers, Tian et al. (2021) found that the lateral growth of the northeastern front of the Tibetan Plateau can be represented with a model incorporating upper crustal overthrusting and lower crustal underthrusting beneath the Liupan Shan area. However, none of these features have been reported by previous portable or permanent broadband seismic studies.

In the following, one type of seismometer named the node geophone from the petroleum industry, which was introduced to the passive source seismic studies, has gradually become the most advantageous option for local exploration surveys. The deployments of large-N experiments within small areas using the node geophones (~100 m) became highly convenient for the 3D detection of shallow crustal structures (Dougherty et al., 2019; Lin et al., 2013). Some laboratory and outdoor experiments even show that node geophones can also be adopted to effectively record teleseismic signals; however, the shortcomings, namely, that they are biased toward relatively high frequencies and are susceptible to local noise and ambient temperatures, limit their use in teleseismic studies (Ringler et al., 2018). Despite this, these geophones have been introduced for traditional teleseismic receiver function analysis (Ward & Lin, 2017), and the results confirm that the recording of nodes can provide good constrains of shallow basin and fault structures (G. Liu et al., 2018; Ward et al., 2018). Simultaneously, node geophones are also used for monitoring traffic, weather, thunder, and blasts in urban seismology (Johnson et al., 2019; Lythgoe et al., 2021).

In this research, we carried out a geophysical survey with a dense linear array of short-period node geophones. This array was oriented north-south connecting the cities of Zhuhai and Lianzhou in Guangdong Province, China (Fig 1 a). From the recording of teleseismic events, we obtained an unprecedentedly detailed stacking profile using the teleseismic receiver function method. With these high-

resolution results, we can provide certain evidence for the existence of remnants from the amalgamation of the East and West Cathaysia blocks.

2 Data and Methods

Using 527 short-period, 3-channel node geophones (Fairfield Zland GEN2 5Hz), we obtained 5.75 TB of seismic waveform data over 37 days from 25 May to 2 July 2019 and a total of 41 Mw 5.5 teleseismic events were recorded (Fig 1 c). Although short-period node geophones are convenient, the quality of the recorded waveforms is greatly affected by the deployment conditions. To ensure that the seismometers are coupled with the earth, node geophones each need to be buried within a 30 cm deep hole and at least 10 cm from the surface, in this way, persistent noise signals at approximately 20~40 Hz can be suppressed (Farrell et al., 2018).

In the early stage, the Python-based seismic tool Obspy was used to process the raw data (Beyreuther et al., 2010). To better constrain the performance of the geophones, we specifically analyzed the filtering parameters by using a series of two-pass, four-pole butterworth filters. Finally, a relatively narrow and low frequency band of 0.02–1 Hz was adopted to avoid the sensitivity of the instrument to high frequencies and prevent the contamination of the teleseismic signals with ambient noise. Upon rotating the three-component waveforms into radial-transverse-vertical (RTZ) coordinates, the direct primary (P-wave) arrival could be clearly distinguished from the continuous waveforms. After applying time-domain iterative deconvolution (Ligorría & Ammon, 1999) and manual checking, a total of 991 teleseismic receiver functions were selected. During the deconvolution process, low-pass Gaussian filters with different Gaussian factors of 2.0, 5.0 and 10.0 were adopted, and the corner frequencies were 1.0, 2.4 and 4.8 Hz, respectively. To avoid the influence of decreasing slowness with increasing conversion depth on the converted waves, the moveout correction method proposed by Yuan et al. (1997) was used to correct each curve to the 65° theoretical curve calculated by the iasp91 velocity model (Kennett & Engdahl, 1991). In the following, according to the piercing points of the Moho-converted phase, hereafter referred to as the Pms phase, the receiver functions with a Gaussian factor of 5.0 were aligned along the profile (Fig 2 a, b). Stacking of receiver functions with Gaussian factors of 2.0 and 10.0 are shown in the Supplementary Materials (Fig S2). In addition, we also binned the receiver functions in each 0.08° grid interval to strength the arrival of the Pms phases. The theoretical Pms arrival times were calculated by the TauP Toolkit (Crotwell et al., 1999) at a depth of 35 km under the iasp91 velocity model. Moreover, to intuitively enhance the signals from multiple waves, we also carried out PmpPms and PmpSms moveout corrections, and the stacking results are shown in Figure 3. During stacking, a smoothing factor was employed to smooth the receiver functions between adjacent grids, while the factor was determined by dividing the amplitude by the square of the distance between two grids. The amplitude and time errors during picking are indicated by the mean value and standard deviation with 100 resamplings according to the 1-dimensional

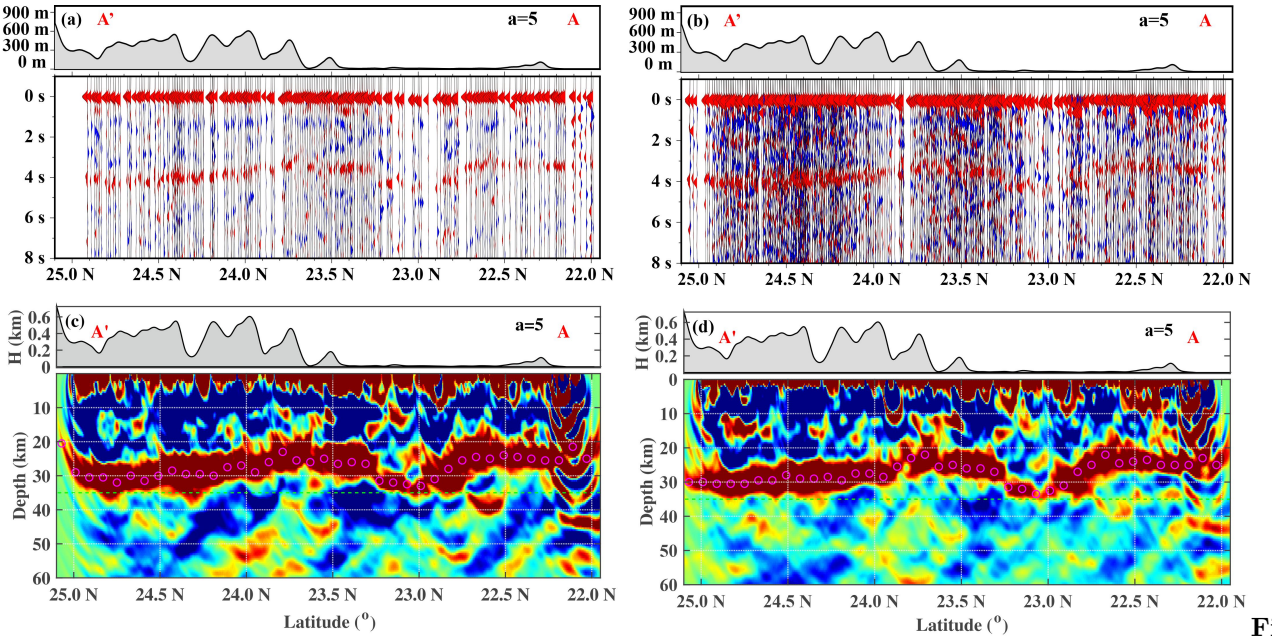

Fi

2. (a) Stacking profile of the single event receiver function with a Gaussian factor of 5.0. (b) Stacking profile of all the teleseismic events receiver function with a Gaussian factor of 5.0. (c) CCP imaging of single event receiver function. (d) CCP imaging of all the teleseismic events receiver function. The CCP imaging results shown with a Gaussian factor of 2.0. The thin green line at 35 km depth represents the Moho depth under the iasp91 model (Kennett & Engdahl, 1991). The thin green dashed lines and pink circles are the theoretical arrival times and observed arrival times of the Pms phase, respectively, which are calculated by the iasp91 velocity model using the 1D time-to-depth conversion method.

For comparison, the receiver functions with high signal to noise ratio from a single Mw 7.3 event at epicentral distance of 35.2° recorded on 24 June 2019 at 02:53:39 UTC is presented in our results (Fig 2 a; Figs S2 a, c). At the same time, the CCP stacking method proposed by Yuan et al. (1997) was adopted to obtain a migrated image along the ray path (Figs 2 c, d and S2).

Combined with a tomographic model, we can also discuss the background S-wave velocity structure with a 0.5° × 0.5° horizontal resolution and 0.2 km vertical resolution over the depth range of 0~180 km (Zhou et al., 2012). Because this tomographic model was calculated from the ambient noise inversion of group and phase velocities, it has a relatively good vertical resolution (Fig S4). In addition, the H–k method was adopted for our research (Zhu & Kanamori, 2000), and the arrival times of the Pms, PmpPms and PmpSms phases were automatically picked after the corresponding moveout correction (Fig 3 a) (Shen et al., 2017).

3 Results

In our results, our focus is on the aligning profiles of receiver functions (Fig 2 and Fig S2). The direct P-wave arrivals are obvious in our results, showing a maximum delay of 0.2 s beneath 23.4~22.5°N, which may be caused by the thick Quaternary sediment at the Sanshui Basin (Fig S1). A secondary positive phase occurs at nearly 3~5 s, which represents the Pms converted wave. The overall trend of Pms converted wave arrivals arriving earlier indicates the slight uplift of the Moho to the southeast. The average arrival times of the Pms, PmpPms and PmpSms phases are 3.8 s, 12.2 s and 14.9 s, respectively, while the corresponding values calculated by the iasp91 velocity model are 4.4 s, 10.9 s, and 13.5 s. The average depth calculated by the H–k method is 30.9 km, while the Moho is deepest (approximately 37 km) beneath 23°N and shallowest (approximately 26 km) beneath 22.5°N. The H–k results show that the average Vp/Vs is approximately 1.78, which is almost the same as the global average (Christensen, 1996). Importantly, Vp/Vs exceeds 1.8 beneath 22.8–23.2°N area, where the maximum Vp/Vs is approximately 1.9 (Fig 3 b).

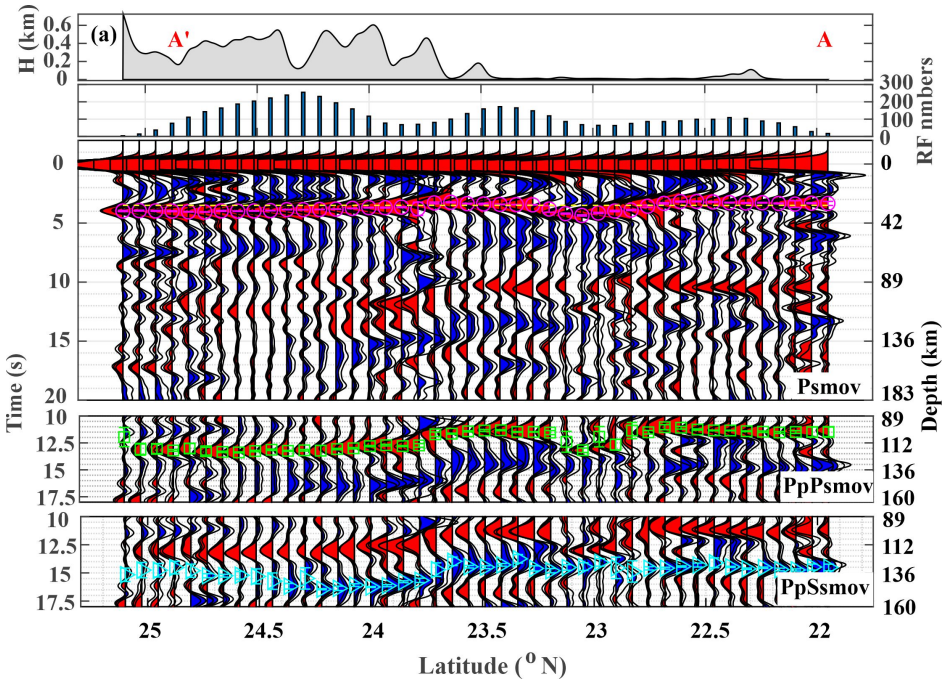

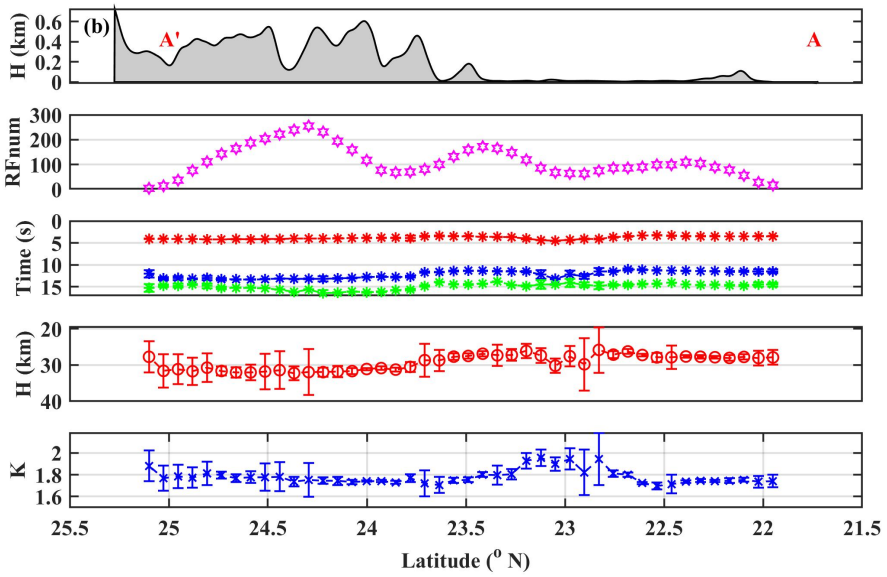

Figure 3. (a) Stacking profile of all the receiver functions after the Pms, PmpPms, PmpSms moveout corrections with a Gaussian factor of 5.0. The solid black line indicates the error during the stacking in each interval, and it is calculated by using the standard deviation with 100 resamplings based on the 1-D bootstrap method. (b) The top panel shows the topographic relief along the profile. The middle two panels are the number of stacked receiver functions and the arrival times of the Pms, PmpPms, and PmpSms phases. The bottom two panels present the crustal thickness and Vp/Vs ratio calculated by the H–k method. The error is indicated by the differences calculated by the H–k method using the arrival times after the Pms and PmpPms moveout corrections. The original data is show in Supplementary materials (Tabel S1).

4 Dicussions

For the exploration of the gold mineralization beneath the Yuegui and Yuezhong blocks, a shorter dense seismic array was oriented in nearly the same direction to us but slightly biased to the west. From the obtained 233 teleseismic receiver functions based on 112 portable EPS-2 short-period seismometers, Li et al. (2021) deducted that a slightly uplifted Moho and the presence of a massive negative phase may be correlated with magmatism and mineralization beneath the Luoding–Yunfu nappe tectonic zone. After acquiring data from another 400 km long wide-angle seismic profile based on six active sources and approximately 54 DZSS-1 seismographs, Zhang et al. (2013) suggested that the Moho east of the Chenzhou–Linwu fault belt is obviously uplifted which can be considered as the convergent boundary bwteen the Yangtz and Cathaysia blocks, while the low P-wave velocity anomalies in this region that may have been caused by an upwelling of hot asthenosphere.. More recently, employing

both active and passive dense seismic arrays with the same starting point as our array (but a southernmost geophone situated more toward the east), Deng et al. (2019) obtained more than 10,000 receiver functions from 2010 to 2015. The most stable feature was a slightly uplifted Moho towards the southeast in their stacking profile. Combined with a velocity model inverted by using surface waves, they found possible lithospheric thinning and the potential upwelling of hot material beneath the centre of Guangdong Province. In another study based on SinoProbe reflection profiling, Dong et al. (2020) found that the structure of the Zhenghe–Dapu fault could be depicted with a stack of parallel reflectors dipping 30° to the northwest. From the above results, it appears that an abnormally weak suture zone may be distributed along the coastal area of the Cathaysia block that is spatially consistent both with the metamorphic core in the Wuyi–Nanling–Yunkai domain distributed along the Zhenghe–Dapu and Gaoyao–Huilai deep faults.

The uplift of the Moho to the southeast in the coastal SCB may be connected to the passive continental margin (Bai et al., 2015). Other evidence indicates that the lithosphere-asthenosphere boundary (LAB) discontinuity also exhibits an uplift trend from the continental margin of the SCB to the northern SCS, and variation of Moho in our profile exhibits the same characteristics as previous results (Tang & Zheng, 2013). In addition, the most obvious feature in our results is the abnormal deepen of Moho beneath 23.5~22.5°N, which can be observed from the aligning profile and CCP imaging with different Gaussian factors (Figs 2, S2, and S3). Simultaneously, multiple converted waves in our results (PmpPms, PmpSms) display a similar pattern as the Pms phase (Fig 3 a). The relatively large Vp/Vs ratio (1.8) beneath the same area may indicate the presence of melt within the crust (Christensen, 1996). The Pms phase beneath 23.7°N shows an offset pattern, and we infer that it may be due to the extension of the deep Gaoyao–Huilai fault, which is served as a deep channel for the upwelling hot materials (Fig 4). Combined with a velocity model (Zhou et al., 2012), it can be observed that hot materials appear to accumulate beneath 23.5°N and 22.5°N (Fig S4). The consistent trend of the negative phase above the deepen Moho supports the upwelling of hot materials along the hot channel beneath approximately 23.7°N (Fig 2 a). The occurrence of the Mw 4.2 earthquake adjacent to this hot channel is evidence of the existence of such a hot channel along the deep fault (Fig 4).

According to the previously reported zircon U–Pb ages of different groups of granitic gneisses, Wang et al. (2014) proposed that the SCB was formed by the amalgamation of various fragments following the episodic closure of a series of northwestern arc-back systems along Wuyi–Yunkai, Shuangxiwu and Jiangnan at ~920 Ma, ~890 Ma, and ~830 Ma, respectively. The collision boundary between the East and West Cathaysia blocks may be an extension of the Zhenghe-Dapu fault, which is connected to the Gaoyao–Huilai fault to the southeast. Under these assumptions, a previous study confirmed that parallel reflectors dipping 30° to the northwest may represent an extension of the Zhenghe–Dapu fault (Dong et al., 2020). From our results, we support the thickened crust

beneath around the Gaoyao-Huilai deep fault, while the relatively large Vp/Vs ratio above the thickened crust may be caused by the upwelling of hot materials. Furthermore, it should be mentioned that these hot materials may have formed by the slab rollback of the subducted Paleo-Pacific plate from the Late Cretaceous to late Cenozoic (Jiang et al., 2015); another possibility is that it was formed by the lateral flow of hot mantle from the Hainan plume (Zhang et al., 2020).

Taking the above considerations, we present a simple model for the variation in the Moho depth beneath the Gaoyao–Huilai and Zhenghe–Dapu faults that may represent the suture zone between the amalgamated East and West Cathaysia blocks. Moreover, the outcrops of metamorphic S-type granites indicate that the amalgamation history is heterogeneous along the two deep faults. Given the lower abundance of metamorphic rocks in the Wuyi–Nanling–Yunkai domain, we deduce that the Nanling domain may be a buffer zone (112–115°N) of the collision between the West and East Cathaysia blocks, as depicted by the pink shading in Figure 1. The Yunkai and Wuyi domains, which are depicted with red shading, may have formed through lithospheric delamination process (Gao et al., 2004) and followed by an intraplate orogeny, represent the severe collision zone of the East and West Cathaysia blocks.

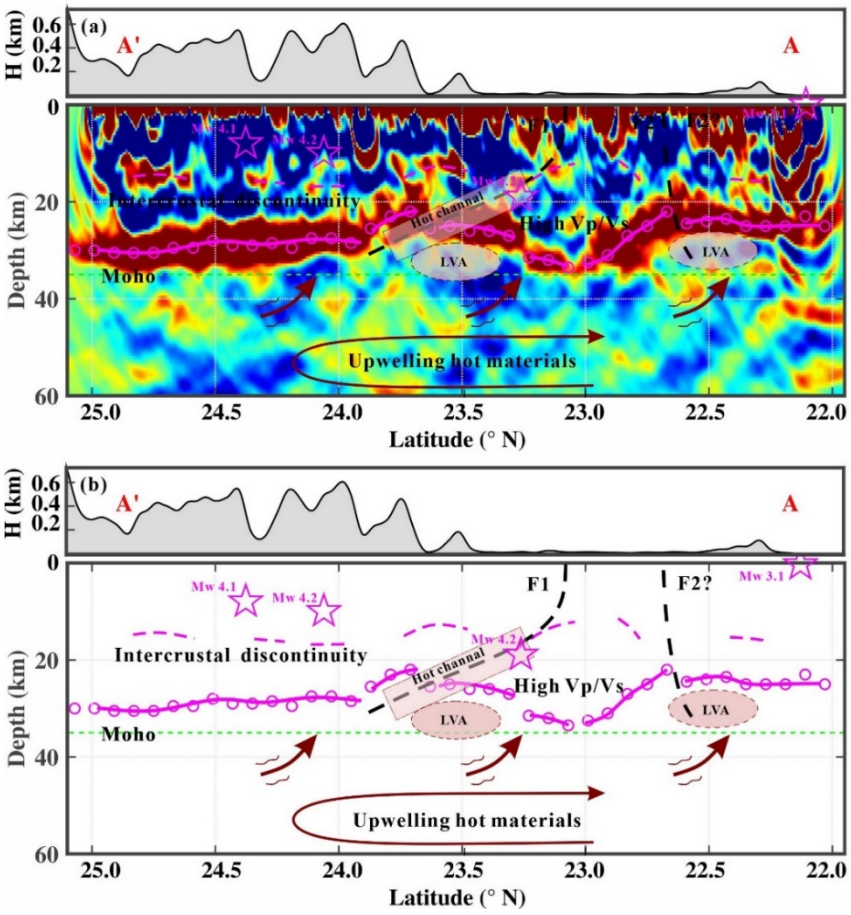

Figure 4. Model of the main crustal structure beneath the profile. (a) The CCP imaging results with a Gaussian factor of 2.0. (b) The main variation in the Moho depth and the interpreted mechanism from the above CCP imaging results. The pink circles are the automatically picked Pms arrivals. The dashed pink line indicates the intracrustal discontinuity. The solid pink line represents the undulating Moho discontinuity. The pink stars represent the local earthquakes downloaded from the IRIS website (http://ds.iris.edu/ds/nodes/dmc/data/types/events/).

5 Conclusions

The main findings from our research are derived from the aligning and migration of teleseismic receiver functions. With the potential discovery of hot upwelling materials along the crustal channel discerned from CCP imaging (Fig 4), we hypothesize that the relatively high Vp/Vs ratio and upwelling of hot materials beneath approximately 23°N may be caused by the retreat of the subducted Pacific slab. Combined with previous results, we deduce that the remnants

of the amalgamation of the West and East Cathaysia blocks can be indicated by the extension of the Gaoyao–Huilai and Zhenghe–Dapu faults through the crustal area. In addition, we establish a simple model for the collision between the East and West Cathaysia blocks along the deep faults. As shown in Figure 5, the amalgamation of these two blocks is constrained to the Neoproterozoic (1000~920 Ma), after which an intraplate orogeny may have dominated during the Paleozoic along the suture zone between the West and East Cathaysia blocks (460–400 Ma) (Fig 5 a). In the mid-Permian (~265 Ma), the Pacific plate started to subduct beneath the Cathaysia block, and in the mid-Paleozoic, it may have experienced a series of slab retreat, rollback and tearing processes (Fig 5 b). From the Jurassic to the Cretaceous, the subducted Pacific slab may have severely foundered, which would have been accompanied by the upwelling of hot materials (Fig 5 c). Therefore, the amalgamation of the East and West Cathaysia blocks together with the upwelling of hot materials played an important role in the formation of the crustal state beneath the deep Gaoyao–Huilai and Zhenghe–Dapu faults.

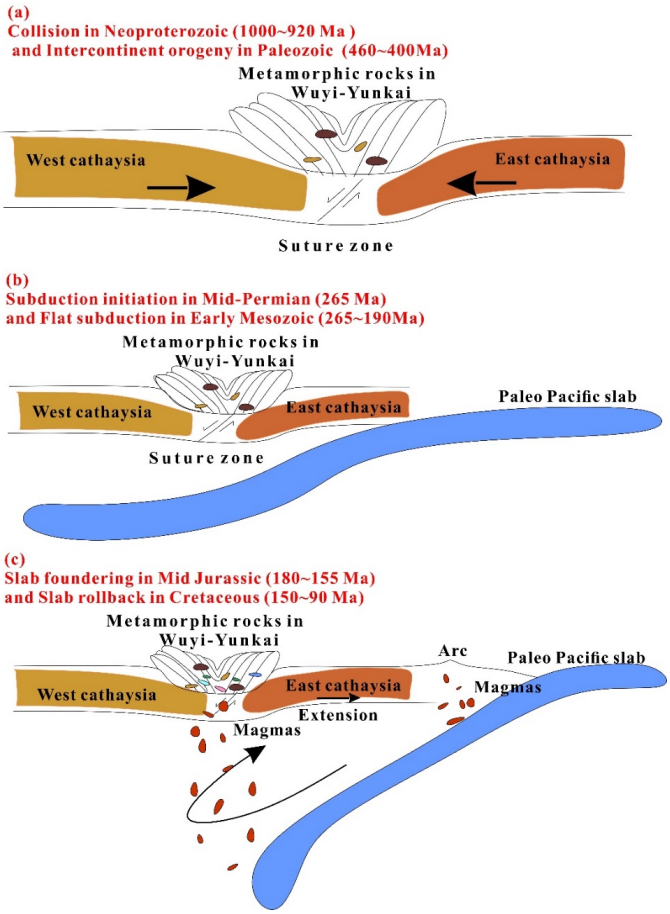

Figure 5. Weak suture zone and subsequent petrogenesis along the deep Gaoyao–Huilai and Zhenghe–Dapu faults. The East and West Cathaysia blocks are represented by brownish yellow and red shading, respectively. The long blue feature represents the subducted Pacific plate. Tiny scattered dots represent metamorphic rocks and upwelling hot materials. The flower structure represents the Wuti–Yunkai orogeny belt.

Acknowledgments

This work has supported by the National Natural Science Foundation of China (Grant 41874052 and 41730212), Guangdong Province Introduced Innovative R&D Team (2017ZT07Z066), the Second Tibetan Plateau Scientific Expedition and Research Program (STEP) (2019QZKK0701), Project supported by Innovation Group Project of Southern Marine Science and Engineering Guangdong Laboratory (Zhuhai) (No. 311021002), Guangdong Collaborative Innovation Center for Earthquake Prevention and Mitigation (2018B020207011).

Open Research

The calculated receiver functions from our research are available from the Zenodo (https://doi.org/10.5281/zenodo.5802538). The tomographic model can be download from the China Geophysical Reference Model website (http://chinageorefmodel.org/china_models_individual/3d_mantle_models).

References

https://doi.org/10.1016/j.tecto.2015.08.028

https://doi.org/10.1785/gssrl.81.3.530

https://doi.org/10.1029/95JB03446

https://doi.org/10.1785/gssrl.70.2.154

https://doi.org/10.1016/j.pepi.2019.04.003

https://doi.org/10.1016/j.epsl.2020.116360

https://doi.org/10.1785/0220190094

https://doi.org/10.1785/0220180073

https://doi.org/10.1038/nature03162

https://doi.org/10.1016/j.lithos.2013.07.002

https://doi.org/10.1080/00206814.2015.1017775

https://doi.org/10.1785/0220180383

https://doi.org/10.1111/j.1365-246X.1991.tb06724.x

https://doi.org/10.1016/j.tecto.2021.229012

https://doi.org/10.1130/g23193a.1

https://doi.org/10.1785/BSSA0890051395

https://doi.org/10.1190/geo2012-0453.1

https://doi.org/10.1785/0220180071

https://doi.org/10.1016/j.lithos.2018.10.006

https://doi.org/10.1093/gji/ggab135

https://doi.org/10.1785/0220170236

https://doi.org/10.1016/j.tecto.2017.06.022

https://doi.org/10.1016/j.tecto.2019.02.002

https://doi.org/10.1016/j.gr.2020.06.018

https://doi.org/10.1016/j.earscirev.2021.103596

https://doi.org/10.1016/j.jseaes.2012.10.037

https://doi.org/10.1016/j.jseaes.2021.104906

https://doi.org/10.1016/j.epsl.2020.116700

https://doi.org/10.1016/j.epsl.2018.06.007

https://doi.org/10.1016/j.gr.2006.10.003

https://doi.org/10.1016/j.precamres.2014.05.003

https://doi.org/10.1029/2018gl079903

https://doi.org/10.1785/0220170051

https://doi.org/10.1002/2017GL075141

https://doi.org/10.1016/j.jseaes.2018.01.012

https://doi.org/10.1029/97JB02379

https://doi.org/10.1002/gj.3533

https://doi.org/10.1016/j.gr.2012.05.018

https://doi.org/10.1016/j.gr.2014.09.004

https://doi.org/10.1016/j.precamres.2012.09.017

https://doi.org/10.1111/j.1365-246X.2012.05423.x

https://doi.org/10.3969/j.issn.1006-7493.2003.04.009

https://doi.org/10.1016/S0012-821X(00)00101-1

https://doi.org/10.1029/1999JB900322

Bai, Y., Wu, S., Liu, Z., Müller, R. D., Williams, S. E., Zahirovic, S., & Dong, D. (2015). Full-fit reconstruction of the South China Sea conjugate margins.

Tectonophysics, 661, 121-135. Beyreuther, M., Barsch, R., Krischer, L., Megies, T., Behr, Y., & Wassermann, J. (2010). ObsPy: A Python Toolbox for Seismology. *Seismological Research Letters, 81*(3), 530-533. Christensen, N. I. (1996). Poisson's ratio and crustal seismology. *Journal of Geophysical Research: Solid Earth, 101*(B2), 3139-3156. Crotwell, H. P., Owens, T. J., & Ritsema, J. (1999). The TauP Toolkit: Flexible Seismic Travel-time and Ray-path Utilities. *Seismological Research Letters, 70*(2), 154-160. Deng, Y. F., Li, J. T., Peng, T. P., Ma, Q., Song, X. D., Sun, X. L., et al. (2019). Lithospheric structure in the Cathaysia block (South China) and its implication for the Late Mesozoic magmatism. *Physics of the Earth and Planetary Interiors, 291*, 24-34. Dong, S., Li, J., Cawood, P. A., Gao, R., Zhang, Y., & Xin, Y. (2020). Mantle influx compensates crustal thinning beneath the Cathaysia Block, South China: Evidence from SINOPROBE reflection profiling. *Earth and Planetary Science Letters, 544*, 116360. Dougherty, S. L., Cochran, E. S., & Harrington, R. M. (2019). The LArge-n Seismic Survey in Oklahoma (LASSO) Experiment. *Seismological Research Letters, 90*(5), 2051-2057. Farrell, J., Wu, S. M., Ward, K., & Lin, F. C. (2018). Persistent Noise Signal in the FairfieldNodal Three-Component 5-Hz Geophones. *Seismological Research Letters, 89*, 1609-1617. Gao, S., Rudnick, R. L., Yuan, H.-L., Liu, X.-M., Liu, Y.-S., Xu, W.-L., et al. (2004). Recycling lower continental crust in the North China craton. *Nature, 432*(7019), 892-897. Huang, X.-L., Yu, Y., Li, J., Tong, L.-X., & Chen, L.-L. (2013). Geochronology and petrogenesis of the early Paleozoic I-type granite in the Taishan area, South China: Middle-lower crustal melting during orogenic collapse. *Lithos, 177*, 268-284. Jiang, Y.-H., Wang, G.-C., Liu, Z., Ni, C.-Y., Qing, L., & Zhang, Q. (2015). Repeated slab advance–retreat of the Palaeo-Pacific plate underneath SE China. *International Geology Review, 57*(4), 472-491. Johnson, C. W., Vernon, F., Nakata, N., & Ben-Zion, Y. (2019). Atmospheric Processes Modulating Noise in Fairfield Nodal 5 Hz Geophones. *Seismological Research Letters*. Kennett, B. L. N., & Engdahl, E. R. (1991). Traveltimes for global earthquake location and phase identification. *Geophysical Journal International, 105*(2), 429-465. Li, X., Li, Z., Xi, Y., Shi, Y., Wang, X., Yan, P., & Bao, F. (2021). High-resolution crustal structure and gold mineralization in the southwest Cathaysia block revealed by a dense seismic array. *Tectonophysics, 816*. Li, Z.-X., & Li, X.-H. (2007). Formation of the 1300-km-wide intracontinental orogen and postorogenic magmatic province in Mesozoic South China: A flat-slab subduction model. *Geology, 35*(2), 179-182. Ligorría, J., & Ammon, C. (1999). Iterative Deconvolution and Receiver-Function Estimation. *Bulletin of the Seismological Society of America, 89*, 1395-1400. Lin, F.-C., li, D., Clayton, R., & Hollis, D. (2013). High-resolution 3D shallow crustal structure in Long Beach, California: Application of ambient noise tomography on a dense seismic array. *GEOPHYSICS, 78*, Q45-Q56. Liu, G., Persaud, P., & Clayton, R. W. (2018). Structure of the Northern Los Angeles Basins Revealed in Teleseismic Receiver Functions from Short-Term Nodal Seismic Arrays. *Seismological Research Letters, 89*(5), 1680-1689. Liu, S., Peng, S., Kusky, T., Polat, A., & Han, Q. (2018). Origin and tectonic implications of an Early Paleozoic (460–440 Ma) subduction-accretion shear zone in the northwestern Yunkai Domain,

South China. *Lithos, 322*, 104-128. Lythgoe, K., Loasby, A., Hidayat, D., & Wei, S. (2021). Seismic event detection in urban Singapore using a nodal array and frequency domain array detector: earthquakes, blasts and thunderquakes. *Geophysical Journal International, 226*(3), 1542-1557. Ringler, A., Anthony, R., Karplus, M., Holland, A., & Wilson, D. (2018). Laboratory Tests of Three Z-Land Fairfield Nodal 5-Hz, Three-Component Sensors. *Seismological Research Letters, 89*. Shen, X., Kim, Y., & Gan, W. (2017). Lithospheric velocity structure of the northeast margin of the Tibetan Plateau: Relevance to continental geodynamics and seismicity. *Tectonophysics, 712-713*, 482-493. Shen, X., Kind, R., Huang, Z., Yuan, X., & Liu, M. (2019). Imaging the Mantle Lithosphere below the China cratons using S-to-p converted waves. *Tectonophysics, 754*, 73-79. Shen, X., Li, Y., Gao, R., Chen, X., Liu, M., Yuan, X., et al. (2020). Lateral growth of NE Tibetan Plateau restricted by the Asian lithosphere: Results from a dense seismic profile. *Gondwana Research, 87*, 238-247. Shu, L., Yao, J., Wang, B., Faure, M., Charvet, J., & Chen, Y. (2021). Neoproterozoic plate tectonic process and Phanerozoic geodynamic evolution of the South China Block. *Earth-Science Reviews, 216*, 103596. Tang, Q., & Zheng, C. (2013). Crust and upper mantle structure and its tectonic implications in the South China Sea and adjacent regions. *Journal of Asian Earth Sciences, 62*, 510-525. Tang, Y.-L., Shi, Y., Hu, X.-M., Liu, X.-J., & Huang, C.-W. (2021). Petrogenesis of Early Paleozoic I-type granitoids in the Wuyi-Yunkai Orogen, South China: Implications for the tectono-magmatic evolution of the Cathaysia Block. *Journal of Asian Earth Sciences, 220*, 104906. Tian, X., Bai, Z., Klemperer, S. L., Liang, X., Liu, Z., Wang, X., et al. (2021). Crustal-scale wedge tectonics at the narrow boundary between the Tibetan Plateau and Ordos block. *Earth and Planetary Science Letters, 554*, 116700. Wang, X., Chen, L., Ai, Y., Xu, T., Jiang, M., Ling, Y., & Gao, Y. (2018). Crustal structure and deformation beneath eastern and northeastern Tibet revealed by P-wave receiver functions. *Earth and Planetary Science Letters, 497*, 69-79. Wang, Y., Fan, W., Zhao, G., Ji, S., & Peng, T. (2007). Zircon U–Pb geochronology of gneissic rocks in the Yunkai massif and its implications on the Caledonian event in the South China Block. *Gondwana Research, 12*(4), 404-416. Wang, Y., Zhang, Y., Fan, W., Geng, H., Zou, H., & Bi, X. (2014). Early Neoproterozoic accretionary assemblage in the Cathaysia Block: Geochronological, Lu–Hf isotopic and geochemical evidence from granitoid gneisses. *Precambrian Research, 249*, 144-161. Ward, K. M., Lin, F., & Schmandt, B. (2018). High-Resolution Receiver Function Imaging Across the Cascadia Subduction Zone Using a Dense Nodal Array. *Geophysical Research Letters, 45*(22). Ward, K. M., & Lin, F. C. (2017). On the Viability of Using Autonomous Three-Component Nodal Geophones to Calculate Teleseismic Ps Receiver Functions with an Application to Old Faithful, Yellowstone. *Seismological Research Letters, 88*(5), 1268-1278. Ye, Z., Li, J., Gao, R., Song, X., Li, Q., Li, Y., et al. (2017). Crustal and Uppermost Mantle Structure Across the Tibet-Qinling Transition Zone in NE Tibet: Implications for Material Extrusion Beneath the Tibetan Plateau. *Geophysical Research Letters, 44*(20), 10,316-310,323. Yu, Y., Huang, X.-L., Sun, M., & He, P.-L. (2018). Petrogenesis of granitoids and associated xenoliths in

the early Paleozoic Baoxu and Enping plutons, South China: Implications for the evolution of the Wuyi-Yunkai intracontinental orogen. *Journal of Asian Earth Sciences, 156*, 59-74. Yuan, X., Ni, J., Kind, R., Mechie, J., & Sandvol, E. (1997). Lithospheric and Upper-mantle Structure of Southern Tibet from a seismological passive source experiment. *Journal of Geophysical Research, 1022*, 27491-27500. Zhang, G., Shao, L., Qiao, P., Cao, L., Pang, X., Zhao, Z., et al. (2020). Cretaceous–Palaeogene sedimentary evolution of the South China Sea region: A preliminary synthesis. *Geological Journal, 55*(4), 2662-2683. Zhang, Z., Xu, T., Zhao, B., & Badal, J. (2013). Systematic variations in seismic velocity and reflection in the crust of Cathaysia: New constraints on intraplate orogeny in the South China continent. *Gondwana Research, 24*(3-4), 902-917. Zhao, G. (2015). Jiangnan Orogen in South China: Developing from divergent double subduction. *Gondwana Research, 27*(3), 1173-1180. Zhao, G., & Cawood, P. A. (2012). Precambrian geology of China. *Precambrian Research, 222-223*, 13-54. Zhou, L., Xie, J., Shen, W., Zheng, Y., Yang, Y., Shi, H., & Ritzwoller, M. H. (2012). The structure of the crust and uppermost mantle beneath South China from ambient noise and earthquake tomography. *Geophysical Journal International, 189*(3), 1565-1583. Zhou, X. (2003). My Thinking about Granite Geneses of South China. *Geological journal of China universities, 9*(4), 556-565. Zhu, L. (2000). Crustal structure across the San Andreas Fault, southern California from teleseismic converted waves. *Earth and Planetary Science Letters, 179*(1), 183-190. Zhu, L., & Kanamori, H. (2000). Moho depth variation in southern California from teleseismic receiver functions. *Journal of Geophysical Research: Solid Earth, 105*(B2), 2969-2980.